

Article

Different Erionite Species Bind Iron into the Structure: A Potential Explanation for Fibrous Erionite Toxicity

Alessandro Pacella ^{1,*}, Carlo Cremisini ², Elisa Nardi ², Maria Rita Montekali ², Ida Pettiti ³, Matteo Giordani ⁴, Michele Mattioli ⁴  and Paolo Ballirano ^{1,5} 

¹ Department of Earth Sciences, Sapienza University of Rome, Piazzale A. Moro 5, I-00185 Rome, Italy; paolo.ballirano@uniroma1.it

² ENEA, Casaccia Research Centre, via Anguillarese 301, S. Maria di Galeria, I-00123 Rome, Italy; carlo.cremisini@enea.it (C.C.); elisa.nardi@enea.it (E.N.); mariarita.monterekali@enea.it (M.R.M.)

³ Department of Chemistry, Sapienza University of Rome, Piazzale A. Moro 5, I-00185 Rome, Italy; ida.pettiti@uniroma1.it

⁴ Department of Pure and Applied Sciences, University of Urbino Carlo Bo, Piazza della Repubblica 13, I-61029 Urbino, PU, Italy; matteo.giordani@uniurb.it (M.G.); michele.mattioli@uniurb.it (M.M.)

⁵ Rectorial Laboratory Fibres and Inorganic Particulate, Sapienza University of Rome, Piazzale A. Moro 5, I-00185 Rome, Italy

* Correspondence: alessandro.pacella@uniroma1.it

Received: 29 December 2017; Accepted: 18 January 2018; Published: 23 January 2018

Abstract: In this investigation, the crystal chemical characterization of one sample of woolly erionite-K (Lander County, NV, USA) was examined after suspension in a FeCl₂ solution, in anaerobic conditions. The aim of this study was to determine the effect of the chemical composition of erionite on its efficiency to bind iron. Inductively coupled plasma (ICP) results showed that the sample bound Fe(II) through an ion-exchange mechanism mainly involving Ca. In addition, chemical and structural data indicated that Fe(II) is fixed at the Ca3 site, six-fold coordinated to water molecules. According to Brunauer–Emmett–Teller (BET) sample surface area the amount of Fe(II) bound by the fibers was comparable with that retrieved for fibrous erionite-Na sample from Rome (OR, USA) for which the ion-exchange process mainly affected Na. This finding provides clear evidence of a strong tendency of Fe(II) to bind to the erionite structure. Furthermore, considering that the woolly erionite-K from Langer County differs markedly from erionite-Na from Rome in the extra-framework cation content, our observations indicate that the Fe binding efficiency is not significantly modulated by the chemical composition. Notably, Fe ion-exchanged and/or accumulated on the fiber surface can generate hydroxyl radicals via the Fenton reaction, thus influencing the potential carcinogenicity of the different erionite species.

Keywords: erionite species; toxicity; Fe(II) binding; cation exchange; ICP-OES

1. Introduction

Erionite is a zeolite often exhibiting fibrous morphology, present as diagenetic alteration of sediments [1], basalts [2], or as a hydrothermal-altered product [3]. Erionite is one of the four ABC-6 family [4] phases characterized by a six-layer sequence (AABAAC erionite: Staples and Gard [5]; AABBC chabazite: Smith et al. [6]; ABBACC bellbergite: Rüdinger et al. [7]; ABABAC liottite: Ballirano et al. [8]). Its framework consists of columns of regularly alternating cancrinite cages, and double 6-rings (D6R) aligned along 0, 0, z and two erionite cages whose axes run along 1/3, 2/3, z, and 2/3, 1/3, z, respectively. The cancrinite and the erionite cages host the extra-framework (EF) cations whereas H₂O is allocated within the erionite cavity. Erionite is hexagonal space group P63/mmc [9]

with an average formula $K_2(Na,Ca_{0.5})_8[Al_{10}Si_{26}O_{72}] \cdot 30H_2O$ [10]. This mineral typically displays a large chemical variability, and for this reason, three species (erionite-Na, erionite-K, and erionite-Ca) were identified depending upon the most abundant EF cation [10–13].

Inhalation of fibrous erionite has shown to be correlated with diseases like those already known from exposure to asbestos [14,15]. In particular, high rates of malignant mesothelioma were reported, since the 1970s, in three villages of Cappadocia, Turkey [16–20]. In vivo and in vitro studies indicated that fibrous erionite is significantly more tumorigenic than chrysotile asbestos and amphibole asbestos [21–26]. As a consequence, the International Agency for Research on Cancer classified erionite as a Group 1 known Human-Carcinogen [27,28]. Natural deposits of erionite, including the fibrous form, were identified in several localities of United States [29]. Further, concerns regarding the human health hazard related to erionite exposure emerged in North Dakota (USA) since 300 miles of roads were surfaced with erionite-containing gravels [19,30,31]. In addition, Baumann et al. [32] discovered that in southern Nevada (USA) erionite deposits encompass large areas where urban development and off-road sport activities resulted in exposure of the local population to this potent carcinogen. Subsequent epidemiological investigations demonstrated several mesothelioma clusters unequivocally associated with erionite exposure in USA [30,33]. Fibrous erionite was also detected in central Mexico and related to enhanced occurrence of mesothelioma cases [34,35]. Further, Ilgren et al. [36] indicated the occurrence of mesothelioma cases in the Iranian village of Kandovan, as well as in other parts of Iran, due to vast amounts of natural zeolites, including fibrous erionite, found in these areas.

It is worthwhile noting that the occurrence of erionite was documented in many altered volcanic and sedimentary deposits globally [1–3]. In Italy, the occurrence of erionite was reported in some areas of Sardinia and Veneto regions [37–39]. Recently, Giordani et al. [26,40] provided a field description and a detailed mineralogical characterization of selected samples of potentially carcinogenic fibrous erionite discovered in the Lessini Mountains (Veneto region, NE Italy).

Although the mechanism by which erionite induces cyto- and geno-toxic damage has not yet been fully elucidated, the toxicity attributed to erionite has been commonly associated with the iron(Fe) ion-exchanged and/or accumulated on its surface, after fiber is deposited within the respiratory epithelium, promoting formation of reactive oxygen species (ROS) by Fenton chemistry [41–45]. Recently, it has been shown that erionite can act as a vehiculating media in the human body for Fe as several Fe-bearing mineral species (nano-oxydes, sulphates, phyllosilicates) were found to adhere at its surface [46,47]. Therefore, these nanoparticles (especially phyllosilicates) can be dissolved during alveolar macrophage phagocytosis, when the fibers are engulfed in the intracellular acidic environment (pH = approximately 4.5), becoming then potential sources of Fe [46,47]. In this regard, Ballirano et al. [48] demonstrated that, whenever erionite fibers are kept in contact with a source of Fe(II), this is ion exchanged and segregated at the Ca3 site within the erionite cavity. Moreover, Fe(III) is predominantly fixed at the surface at relatively high concentration, whereas at low concentrations typical of body fluids, it is primarily segregated at the Ca3 site within the erionite cavity, similarly to ferrous iron [49].

Recently, Pacella et al. [50] further explored the Fe binding process using a sample of erionite-Na after K-loading. The K-exchanged sample exhibited a 95% reduction of the Brunauer–Emmett–Teller (BET) surface area indicating that upon treatment the sample behaves as a mesoporous material, in agreement with Eberly [51]. Surprisingly, despite the large potassium (K) ions blocked off nearly all pores, erionite-K retains its capacity of binding Fe(II) in the erionite cavity by ionic exchange, with efficiency comparable to that observed for the pristine sample (erionite-Na). Although it is not yet known which erionite species is most likely to induce mesothelioma in a given locality, evidence indicates the limited effect of the chemical composition of erionite on Fe binding process and suggests that toxicity attributed to erionite may be considered independent of its chemical composition.

The present study was undertaken to provide a detailed crystal chemical and structural characterization of a sample of erionite-K after suspension in $FeCl_2$ solution. This study aimed at further investigating the effect of erionite chemical composition on its efficiency to bind Fe.

On this basis, results obtained may provide a rationale for future experiments to shed new light on erionite-mediated toxicity and carcinogenicity.

2. Materials and Methods

2.1. Sample Description

The sample investigated in this work was woolly erionite from the locality of Lander County (NV, USA), which is commonly found in poorly exposed brownish-grey mudstone of unknown thickness, stratigraphically located just beneath a 1-m-thick conspicuous grey vitric tuff [52]. Recently, Mattioli et al. [53] identified the chemical composition of this sample by Scanning Electron Microscopy equipped with Energy Dispersive X-ray System (SEM/EDS) and the sample was classified as erionite-K, according to its crystal-chemical formula $\text{Ca}_{1.72}\text{Na}_{0.74}\text{K}_{2.56}\text{Mg}_{0.35}[\text{Al}_{8.08}\text{Si}_{28.05}\text{O}_{72}]\cdot 29\text{H}_2\text{O}$. As reported by Mattioli et al. [53], the hand specimen consists of thin, hair-like fibers with a diameter ranging from 0.5 to 3 μm and extremely variable lengths, up to 200–300 μm (Figure 1), characterized by a snow-white color and pearly luster, identical in appearance to the type present in the locality of Durkee (OR, USA). Bundles of fibers were picked up under a binocular microscope to obtain a nearly pure sample. However, X-ray powder diffraction (XPRD) investigation of the sample revealed the presence of traces of quartz and calcite.

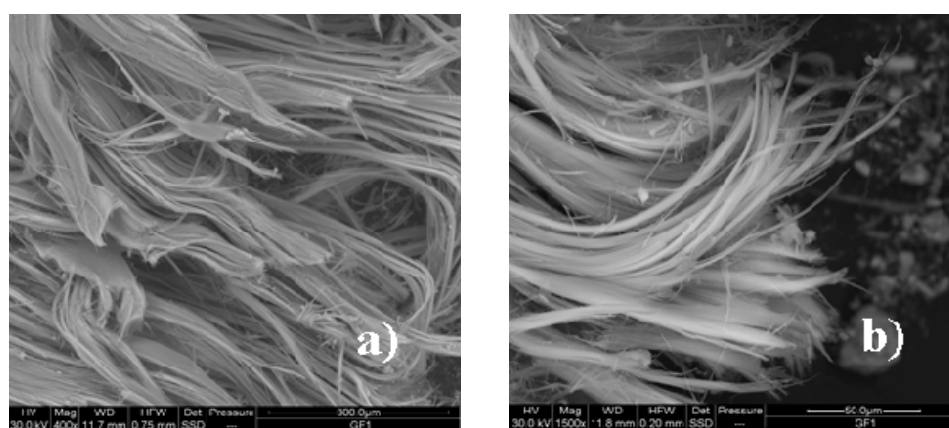


Figure 1. SEM images of the woolly erionite from Lander County (NV, USA): (a) Dimension bar 300 μm ; (b) dimension bar 50 μm .

2.2. Fe(II) Binding to Erionite

A 10,000 μM FeCl_2 solution was initially prepared dissolving 1.2 g of FeCl_2 (80 mesh, 98%, Sigma-Aldrich, Saint Louis, MO, USA) in 1 L of deionized water (18 Mohm cm at 25 $^\circ\text{C}$, from a Millipore MilliQ Element System, Merck KGaA, Darmstadt, Germany) previously purged with nitrogen to remove oxygen, to prevent the formation of hydroxides and/or oxy-hydroxides. The presence of Fe(III) in the reagent grade FeCl_2 powder was preliminarily ruled out by Mössbauer spectroscopy. Later, the 10,000 μM FeCl_2 solution was diluted using nitrogen purged deionized water to obtain the concentration of 500 μM used in our experiments. All dilutions were performed in a nitrogen-filled glove-bag to further prevent the formation of hydroxides and/or oxy-hydroxides. In addition, pH measurements were conducted (pH ca. 5) using a portable 250A Orion pH Instrument (Thermo Electron Corp., Beverly, MA, USA) equipped with an Orion gel-filled combination pH-electrode (Thermo Electron Corp., Beverly, MA, USA). Fe(II) binding to erionite experiments were performed following the same procedure of Ballirano et al. [48]. In particular, 25 mg erionite fibers were suspended in 25 mL FeCl_2 solution in a 50 mL FalconTM polypropylene tube (VWR Int., Radnor, PA, USA). All sample suspensions were prepared in the nitrogen-filled glove-bag. Moreover, blank samples were prepared by suspending fibers in deionized water, adjusted to the appropriate pH (ca. 5) with addition

of HCl (Ultrex II, ultrapure reagent, JT Baker, Phillipsburg, NJ, USA). Notably, due to the complexity of the task and to reduce the number of variables to be controlled during experiments we have chosen a simplified system exclusively mimicking pH conditions compatible with those found within the lung (pH ca. 4.5 during alveolar macrophage phagocytosis). This choice is justified by the will of employing a simple solution, from the chemical point of view, owing to the ion-exchange property of the zeolite. Further, to model in detail the behavior of erionite whenever in contact with a source of Fe(II), we have explored a Fe concentration well above that found within the human body (Gutteridge et al. [54] reported a total Fe content as small as $0.21(4) \mu\text{mol}\cdot\text{L}^{-1}$ for bronchoalveolar lavage of normal humans). As soon as suspensions were prepared, all polypropylene tubes, closed and sealed with Parafilm® (Sigma-Aldrich, Saint Louis, MO, USA), were removed from the glove-bag and placed in an oscillating bath at room temperature (25 °C) for 1 h. Next, tubes were placed again in the oxygen-free glove bag and supernatant solution was sampled and filtered, using a $0.22 \mu\text{m}$ nitrocellulose membrane filter, for ICP-OES analysis. The fibers were recovered from the tube on filter, rinsed with ultrapure deionized water to remove any residues of Fe not bound, dried and stored under nitrogen prior to the SEM-EDS and XRPD measurements.

2.3. ICP-OES Analysis

One mL of each filtered solution was diluted (1:10) with 1% nitric acid solution and analyzed by ICP-OES to measure concentrations of Ca, Mg, Na, K, Si, Al, released from the fibers, and remaining Fe concentration in solution after fiber suspension. All measurements were performed using an Optima 2000 DV ICP-OES spectrometer (Perkin-Elmer, Norwalk, CT, USA), equipped with a cross flow nebulizer placed inside a Scott spray chamber. ICP Aristar (BDH) standard solutions in nitric acid were employed to prepare the calibrating solutions for ICP-OES analysis of Ca, Na, Mg, K, Si, Al and Fe. To ensure adequate quality, the measures of the standard solutions were regularly repeated after the measurements of a defined number of samples. Controls of incubation of FeCl_2 solution without erionite were also carried out and no changes in Fe concentration were detected.

ICP results of released cations and acquired Fe by erionite fibers are presented as nmol/mg erionite. To determine the net cation release during incubation of the sample in FeCl_2 solution, values measured after suspension in the FeCl_2 solution were subtracted by levels measured in the blank procedure (suspension of fibers in water at the appropriate pH). The amount of Fe bound by erionite was calculated by difference between Fe concentration determined in the initial solution and that measured in the solution after 1 h sample incubation. Due to admixed Fe-bearing impurities within the sample, controls on Fe release during incubation of erionite fibers in water were also performed and no Fe release was detected. Finally, as reported by Ballirano et al. [48] and Pacella et al. [50], a charge balance was retrieved, comparing the net charges released into solution to total charges acquired under the form of Fe.

2.4. Surface Area Measurement

Surface area, Brunauer–Emmett–Teller (BET) multipoint method [55], and textural analysis were obtained by N_2 adsorption/desorption measurements at the liquid nitrogen temperature ($-196 \text{ }^\circ\text{C}$), using a 3-Flex analyzer (Micromeritics, Norcross, GA, USA). Before analysis, the sample was pre-treated at $120 \text{ }^\circ\text{C}$ for 3 days and then at $150 \text{ }^\circ\text{C}$ for other 3 days as water desorption from micropores was difficult. The pores distribution was determined from the adsorption curve by the Barret–Joyner–Halenda (BJH) method [56] and from the analysis of the micropore isotherm by the *t*-test [57] taking the curve of Harkins and Jura [58]. The total pore volume was determined by the rule of Gurvitsch [59].

2.5. SEM-EDS

The micro-chemical characterization was performed using a Quanta 400 SEM (FEI, Hillsboro, OR, USA) equipped with an EDX Genesis EDS system. Operating conditions were: 15 kV accelerating

voltage, 11 mm working distance, 0° tilt angle. Chemical data were collected at least at 8 analytical points. Water content of the pristine sample was determined by thermogravimetric (TG) analysis. Data were collected in the 299–1273 K temperature range, at a heating rate of 10 K·min⁻¹. The sample was placed in an alumina crucible and the analysis was performed, under a constant aseptic air, using a Netzsch STA 449 C Jupiter (Selb, Germany). The final crystal chemical formula was calculated on the basis of 36 [Si + Al + Fe(III)] *apfu*, after renormalization of the chemical analyses to the water content of 21.55 wt % determined by TG.

Both the balance error formula E% [60] and the K content filter [61] were used for the selection of the positive analyses. Indeed, the original E% formula was modified as follow: in order to include in the calculation the Fe(II) loaded by erionite.

2.6. XRPD

Bundles of fibers were disaggregated with a needle, loaded in a 0.7 mm diameter borosilicate glass-capillary, and mounted and aligned onto a standard goniometer head. Analyses were collected with a D8 Advance (Bruker AXS, Karlsruhe, Germany) equipped with focusing Göbel mirrors placed along the incident beam and a position sensitive detector VANTEC-1, operating with a detector window of 6° and fitted with radial Soller slits. Diffraction patterns were measured in step-scan mode in the 6°–145° 2θ angular range, step size of 0.022° 2θ, and counting time of 10 sec. Experimental details of the XRPD data collection are reported in the Supplementary Material (Table S1). Structure refinements were performed by the Rietveld method using Topas 4.2 software [62]. Starting structural data of erionite were extracted from Ballirano et al. [63] following the same refinement strategy. The ellipsoid modeling of the average shape of nanosized crystallites, proposed by Katerinopoulou et al. [64] was applied, owing to the strongly anisotropic shape of the crystallites arising from fiber curling [61]. The anisotropic shape and fiber curling produce significant broadening of the various Bragg reflections depending on the orientation of the diffraction vector. Absorption of a cylindrical sample was refined following the formulae supplied by Sabine et al. [65] and the approach of Ballirano and Maras [66] was used to cope with correlation between displacement parameters and absorption. Preferred orientation was modeled using spherical harmonics (sixth-order, 8 refinable parameters) by selecting the number of appropriate terms as suggested by Ballirano [67]. Full structural data of the samples were submitted as CIF files in the Supplementary Material. Conventional Rietveld plots are reported in Figure 2.

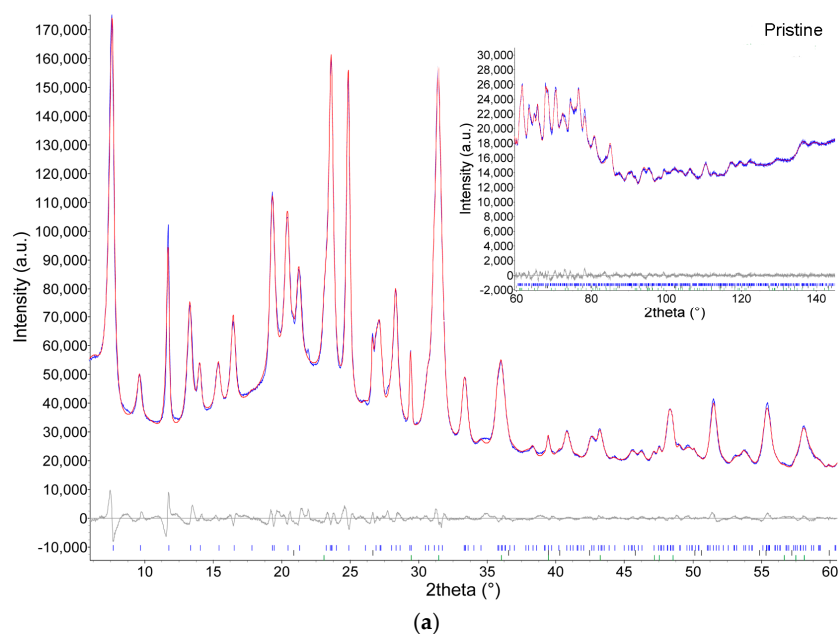


Figure 2. Cont.

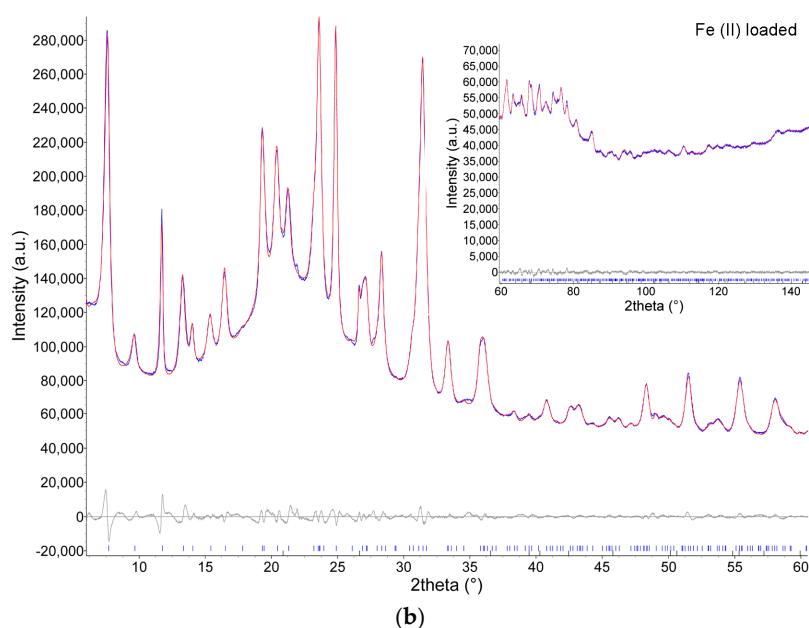


Figure 2. Magnified view (6° – 60° 2θ) of the conventional Rietveld plots of the refinements of (a) pristine and (b) Fe(II) loaded erionite samples. Inset: 60° – 145° 2θ angular range. Experimental (dots), calculated (solid line) and difference plots (below) are shown. Vertical bars refer to the position of calculated Bragg reflections of, from above to below, (a) erionite, quartz, calcite and (b) erionite, quartz.

3. Results

3.1. Fe(II) Binding to Erionite and Chemical Characterization

ICP data indicated that erionite from Nevada bound 367(22) nmol/mg Fe after suspension in the 500 μ M FeCl₂ solution. As presented in Table 1, K and Ca are the extra-framework cations predominantly released during incubation of erionite in water at pH (ca. 5). Moreover, leaching of Ca and Mg markedly increased during fiber suspension in 500 μ M FeCl₂ solution, as compared to that observed in water (Table 1). The net charge released was nearly equal to that acquired under the form of Fe(II) (Table 2), demonstrating that erionite bound Fe(II) by an ion-exchange process involving mainly Ca among the extra-framework cations. However, a charge discrepancy of 97 e[−] was observed. Notably, Eborn and Aust [42] and Pacella et al. [49] have shown that the presence of extra-charge under the form of Fe indicates that Fe is not bound within the erionite structure primarily by ion-exchange, but is fixed at the fiber surface as oxy-hydroxides. On this basis, although the FeCl₂ solution was prepared in a nitrogen-filled glove-bag to prevent the Fe(II) oxidation occurring during fiber incubation, a small amount of Fe(III) was also deposited on the fiber surface as oxy-hydroxides accounting for approximately 10% of the total acquired Fe (Table 2).

Interestingly, Ballirano et al. [48] showed that both erionite-Na from Rome (OR, USA) and woolly erionite-K from Durkee (OR, USA) could fix Fe(II) into the structure through ion-exchange involving mainly Na. Further, the amount of Fe(II) bound by sample in this study [330(20) nmol/mg] is comparable with that acquired, under the same experimental conditions, by erionite-Na from Rome (OR, USA) [262(1) nmol/mg]. These data are relevant considering the reported higher selectivity of erionite for Ca with respect to Na [68,69], and provide evidence of a strong tendency of Fe(II) to enter the erionite structure, due to its relatively high ionic potential, which exceeds that of the common extra-framework cations [50]. In agreement, Erdem et al. [70] suggested that the selectivity sequence $\text{Co}^{2+} > \text{Cu}^{2+} > \text{Zn}^{2+} > \text{Mn}^{2+}$, observed in natural zeolites, is directly related to the charge density of the heavy metal cations. In addition, the limited content of exchanged K measured for all erionite

samples (Tables 1 and 2) may be due to steric hindrance, as each cancrinite cavity contains one K ion that cannot be removed and replaced without destabilizing the structure.

Table 1. ICP analyses of the supernatants for cation release. Cation release is reported as nmol/mg of sample. In addition, data of woolly erionite-K from Durkee (OR, USA) and erionite-Na from Rome (OR, USA) are reported for comparison [48].

Cation Release nmol/mg	H ₂ O (pH Approximately 5)			500 μ M FeCl ₂		
	Lander County	Durkee	Rome	Lander County	Durkee	Rome
Mg	2(0)	-	-	28(2)	13	5(0)
Ca	14(4) *	1	-	275(14)	25	14(1) **
Na	7(1)	68	42(0)	17(2)	364	515(2)
K	17(2)	3	2(0)	67(5)	15	44(1)

Note: * Ca release of sample from Lander County is also due to the dissolution at acidic pH of traces of admixed calcite. ** Ca release of sample from Rome is due to the presence of traces of admixed chabazite [48], being Ca absent in the erionite fibers as indicated by SEM-EDS analysis (Table 3).

Table 2. Charge balance involved in the cation exchange process. In addition, data of woolly erionite-K from Durkee (OR, USA) and erionite-Na from Rome (OR, USA) are reported for comparison [48].

Net Released Charge (e ⁻)	Lander County	Durkee	Rome
Mg	53(4)	27	10(0)
Ca	522(21)	47	-
Na	10(2)	296	473(2)
K	51(3)	13	42(1)
Total	636(29)	382	525(3)
Acquired charge (Fe)	733(45)	440	582(3)
Acquired charge (90% Fe ²⁺)	660(40)	396	523(2)

Note: Ca charge of sample from Rome was not considered in the calculation of the net released charge because is due to the presence of chabazite traces [48], being Ca absent in the fibers as indicated by SEM-EDS analysis (see Table 3).

The chemical composition of the pristine sample agrees with that reported by Mattioli et al. [53] from the same hand specimen and with that noted by Gude and Sheppard [52] for a sample from the same locality (Table 3). However, in our case the EDS spectra obtained on isolated fiber bundles indicated the absence of Fe. Therefore, the presence of this element in the erionite fibers was ruled out and the small amount of FeO measured by Gude and Sheppard [52] and Mattioli et al. [53] may be attributed to impurities.

The calculated crystal chemical formula of pristine sample enables its classification as erionite-K, similarly to woolly erionite from Durkee examined by Ballirano et al. [48] (Figure 3). However, as shown in Table 3, erionite from Lander County has a Na₂O content of approximately 0.75 wt % (corresponding to 0.73 *apfu* Na), which is markedly lower than that measured for Durkee erionite (approximately 2.19 wt %, corresponding to 2.04 *apfu* Na).

The chemical analysis of the fibers suspended in FeCl₂ solution indicated a content of 1.2 wt % FeO [corresponding to 0.51 *apfu* Fe(II)] in the fibers (Table 3). However, the FeO content measured by SEM-EDS does not perfectly match ICP findings [estimated to ca. 1.1 *apfu* Fe(II)], being comparable or even lower than that observed by Ballirano et al. [48] for erionite from Durkee and Rome (OR, USA) (see Tables 2 and 3). In addition, in the case of the present sample, SEM-EDS was not able to detect any significant differences between extra-framework cations content pre- and post-FeCl₂ incubation.

Table 3. SEM-EDS chemical analyses of the both pristine and after FeCl₂ incubated erionite samples from Langer County (NV, USA). In addition, data of woolly erionite-K from Durkee (OR, USA) and erionite-Na from Rome (OR, USA) are reported for comparison [48]. Both R and extra-framework electron density (i.e., site scattering, s.s.), as derived from Rietveld refinements are reported for comparison. The E% original formula by Passaglia [60] has been modified as follow, to keep into account the extra-framework Fe(II) content: $E\% = \frac{[Al+Fe(III)] \cdot \{[Na+K]+2[Mg+Ca+Sr+Ba+Fe(II)]\}}{\{[Na+K]+2[Mg+Ca+Sr+Ba+Fe(II)]\}}$. M = (Na + K); D = (Mg + Ca + Fe).

Oxides (wt %)	Lander County		Lander County		Durkee		Rome	
	Pristine	500 μM FeCl ₂	Mattioli et al. [53]	Gude and Sheppard [52]	Pristine	500 μM FeCl ₂	Pristine	500 μM FeCl ₂
SiO ₂	55.65(35)	55.21(35)	58.47(35)	58.02	58.91(26)	58.77(31)	60.06(47)	59.62(21)
Al ₂ O ₃	13.96(17)	13.88(13)	14.30(21)	14.47	13.54(15)	13.46(23)	12.81(19)	12.57(36)
Na ₂ O	0.75(16)	0.54(8)	0.80(10)	1.08	2.19(20)	1.14(16)	4.03(27)	2.76(41)
K ₂ O	3.96(19)	3.73(19)	4.17(29)	4.64	3.63(24)	3.31(27)	4.01(42)	3.70(38)
MgO	0.34(9)	0.28(8)	0.48(12)	0.42	0.71(10)	0.63(8)	0.59(24)	0.64(25)
CaO	3.80(36)	3.61(23)	3.35(23)	3.29	2.51(22)	2.38(15)	-	-
FeO	-	1.20(39)	0.12(4)	0.21	-	1.79(24)	-	2.21(20)
H ₂ O	21.55 *	21.55 *	18.46(45)	17.82	18.50	18.50	18.50	18.50
Total	100.00	100.00	100.15	99.41	99.99	99.98	100.00	100.00
Si	27.78(9)	27.76(6)	28.05(10)	27.81	28.32(7)	28.34(11)	28.76(11)	28.83(19)
Al	8.22(9)	8.24(6)	8.08(12)	8.19	7.68(7)	7.66(11)	7.24(11)	7.17(19)
Na	0.73(15)	0.53(8)	0.74(10)	1.00	2.04(19)	1.07(15)	3.75(27)	2.59(39)
K	2.52(13)	2.40(13)	2.55(18)	2.84	2.23(15)	2.04(17)	2.45(27)	2.29(24)
Mg	0.26(7)	0.21(6)	0.35(9)	0.30	0.51(7)	0.46(6)	0.42(17)	0.46(18)
Ca	2.03(20)	1.95(13)	1.72(12)	1.69	1.30(12)	1.23(8)	-	-
Fe	-	0.51(17)	0.05(2)	0.08	-	0.72(10)	-	0.90(8)
O	71.80(23)	72.01(21)	71.72	71.91	72.10(14)	72.14(22)	72.10(14)	72.21(17)
H ₂ O	35.95(20)	36.22(21)	29.54(77)	28.55	29.72(12)	29.82(16)	29.60(17)	29.90(10)
E%	5.3	0.1	7.04	2.3	-2.5	-3.3	3.1	5.3
R	0.772(2)	0.771(2)	0.776	0.773	0.787(2)	0.787(3)	0.799(3)	0.801(5)
M/(M + D)	0.587(32)	0.524(26)	0.609	0.649	0.703(14)	0.563(23)	0.936(27)	0.782(45)

Note: * measured by TG/DSC analyses (Ballirano et al. [71]).

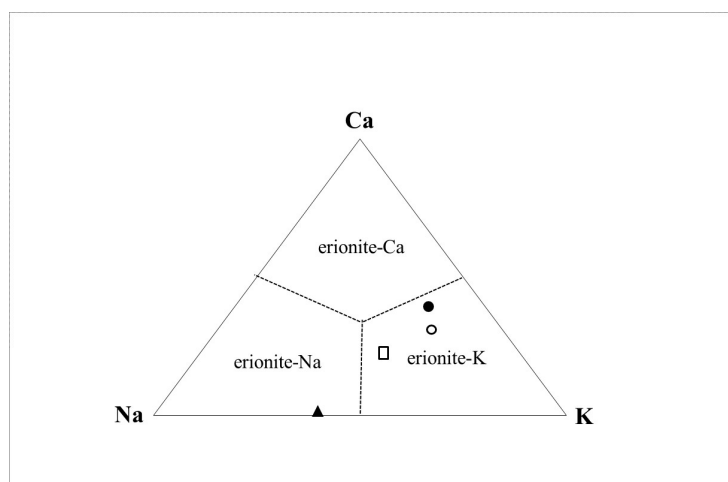


Figure 3. Erionite compositions in atomic percentage for Na, K, and Ca. Solid circle: woolly erionite from Lander County (NV, USA) of this work; open circle: woolly erionite from Lander County (NV, USA) of Gude and Sheppard [52]; triangle: erionite from Rome (OR, USA) of Ballirano et al. [48]; square: woolly erionite from Durkee (OR, USA) of Ballirano et al. [48].

3.2. Structural Modifications

Cell parameters of pristine material are $a = 13.2560(4) \text{ \AA}$, $c = 15.0473(5) \text{ \AA}$, leading to a volume of $2289.90(15) \text{ \AA}^3$. The c/a ratio is of 1.1351. Following the regression equation of Giordani et al. [40] the volume is consistent with an $R = \left(\frac{\text{Si}}{\text{Si}+\text{Al}}\right)$ value of 0.784 in reasonable agreement with 0.772 from SEM-EDS data. Upon Fe(II) loading the a -parameter expands slightly to $13.2627(4) \text{ \AA}$ whereas the c -parameter contracts to $15.0409(5) \text{ \AA}$, leading to a reduction of the c/a ratio to 1.1341 (Supplementary Material, Table S2). This is essentially the same behavior reported for both woolly erionite-Na from Durkee and erionite-Na from Rome, OR, USA [48]. Microstructural parameters (ϵ_0 microstrain and anisotropic crystallite shape) were retrieved from the analysis of the peak broadening. In particular, the anisotropic crystallite size was described by means of the r_a and r_c principal radii of an ellipsoid oriented with the c -axis parallel to the fiber elongation and the a -axis perpendicular to the fiber elongation. Data indicate a significant microstrain of approximately 0.2 similar in magnitude to that reported by Cametti et al. [61] and Ballirano et al. [48] for woolly erionite-Na and -K from Durkee, respectively. Such large values are clearly related to fibers curling. Microstrain is partly released after Fe(II) loading because of a partial dissolution of fibers occurring in the acidic solution, as indicated by the reduction of the refined principal r_a radius (Supplementary Material, Table S2). The framework of pristine sample is characterized by $\langle \text{T1-O} \rangle$ and $\langle \text{T2-O} \rangle$ bond distances of 1.6279 \AA and 1.6465 \AA respectively (Supplementary Material, Table S3) that are only marginally different in the case of the Fe(II) loaded sample possibly owing to protonation [49]. The $R = \left(\frac{\text{Si}}{\text{Si}+\text{Al}}\right)$ values, based on the Jones [72] determinative curves, are higher than those arising from the regression equation of Giordani et al. [40]. This is possibly due to the extreme sensitivity of those curves from small variations of average T1-O and T2-O distances that may be attributed to the detrimental effects of an imperfect peak-shape modeling in the case of curled fibers [61]. Fractional coordinates, displacement parameters and site scattering (s.s.) of extra-framework cation sites and water molecules sites are reported in Table 4. It is worth mentioning that s.s. indicates the number of electrons residing at a particular structural site and that this parameter may be used for identifying the cation species populating the site itself. All refined parameters are only marginally different before and after Fe(II) loading. This fact is related to the relatively limited extension of the Fe(II) * Na ion exchange process. Similarly to woolly erionite from Durkee, extra-framework cations are allocated at Ca1, Ca2, Ca3 sites (within the erionite cavity, see Figure 4), and at K1 site (within the cancrinite cage). No electron density was detected at K2 site even though SEM-EDS indicates a content exceeding the 2 *apfu* K that are located within

the 2 cancrinite cages of the structure. Recently, Pacella et al. [50] found additional K ions at (near) positions occupied by water molecules (OW sites) and at Ca2 site in the case of a K-exchanged erionite sample. Accordingly, it may be expected that the K ions exceeding 2 *apfu* may be located at the same sites. However, analysis of ligands around the Ca2 site (Table 5) did not reveal occurrence of a suitable coordination polyhedron for K, differently from the K-exchanged sample characterized by Pacella et al. [50]. Therefore, it seems reasonable that additional K ions are located at (near) OW sites. Regarding the site partition, following reference data all Ca was allocated at Ca2 and Ca3 sites whereas Na and Mg were located at Ca1 site (Figure 4). However, similarly to other structure refinements of erionite fibers, the total s.s. at the extra-framework cation sites was significantly higher than that obtained from SEM-EDS data. Pacella et al. [73] demonstrated that this is an effect of alkali migration, prevalently Na, occurring during EDS analyses. It may be noted that Ca1 site (a) is the most loaded extra-framework cation site and (b) is the only one showing an increase of s.s. upon Fe(II) loading, passing from 26.5(11) to 30.1(12) e^- . The interpretation of this behavior is not trivial as reference data [48,50] indicate that Fe tends to segregate at Ca3 site. Differently, in this case the increase of s.s. at Ca1 site may suggest a preferential partition at Ca1. However, (Table 5) no acceptable coordination for Fe(II) is observed at this site. A possible alternative interpretation might be that Fe(II) is fixed at Ca3 site and that simultaneously Ca is mobilized from Ca3 toward the neighbor Ca1 site where Na is partly released. It is worthwhile noting that the 6-fold coordination for Fe(II) at Ca3 site is less regular than that detected by Ballirano et al. [48] in more Fe-loaded samples. In fact, in the present case Ca3 site is coordinated to $3 \times$ OW10 at 2.34(2) Å and to $3 \times$ OW7 at 2.38(2) Å. Both distances are larger than expected in the case of the presence of Fe(II) (approximately 2.15–2.2 Å) but this is because the position of Ca3 site represents an average of that occupied by two significantly different cations in terms of dimension (Fe and Ca). In the case of the experiments reported by Ballirano et al. [48], Fe was largely the most abundant cation allocated at Ca3 site, therefore the average position represented in effect that of Fe. In contrast, in the present case Ca contributed heavily in terms of site scattering and the average site position is intermediate between those occupied by the two cations.

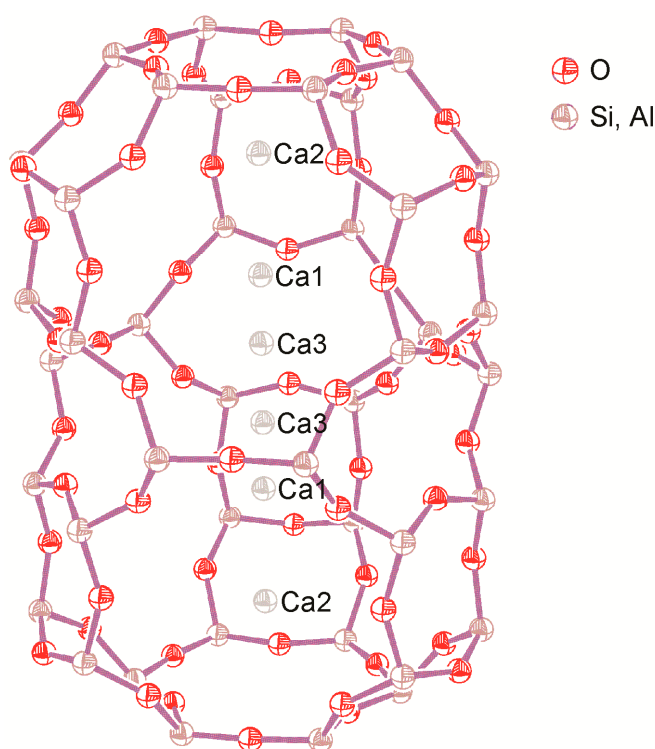


Figure 4. ORTEP-3 plot [74] of the erionite cage showing the Ca1, Ca2, and Ca3 sites.

Table 4. Fractional coordinates, displacement parameters (Biso), site scattering from refinement (s.s. ref.), site scattering from electron density (i.e., site partition, s.s. part.), expressed as e⁻, of extra-framework cations and water molecules of pristine and Fe(II) loaded samples.

Pristine							
Site	x	y	z	B _{iso}	s.s. Ref.	Site Partition	s.s. Part.
Ca1	1/3	2/3	0.923(2)	10.7(8)	26.5(11)	Mg _{0.26} Na _{0.73} Ca _{0.08}	12.8
Ca2	1/3	2/3	0.086(2)	10.7(8)	18.8(9)	Ca _{0.94}	18.8
Ca3	1/3	2/3	0.6896(16)	10.7(8)	20.3(7)	Ca _{1.01}	20.2
K1	0	0	1/4	2.43(19)	38	K _{2.00}	38
Σ _{EF cations}					104(3)		90
OW7	0.2361(9)	2x	3/4	5.5(2)	40.4(7)		
OW8	0.2583(13)	2x	0.036(2)	10.9(4)	38.2(11)		
OW9	0.488(2)	2x	0.948(4)	10.9(4)	32(3)		
OW10	0.4353(8)	2x	0.6737(11)	10.9(4)	63.4(12)	K _{0.52}	9.9
OW11	0.2575(18)	2x	0.588(2)	10.9(4)	39.6(17)		
OW12	0.4300(11)	2x	0.0032(13)	10.9(4)	64.4(17)		
Σ _{water mol.}					278(9)		
500 μM FeCl ₂							
Site	x	y	z	B _{iso}	s.s. Ref.	Partition	s.s. Ref.
Ca1	1/3	2/3	0.9264(19)	12.4(9)	30.1(12)	Mg _{0.21} Na _{0.53} Ca _{0.64}	21.2
Ca2	1/3	2/3	0.083(2)	12.4(9)	19.2(10)	Ca _{0.96}	19.2
Ca3	1/3	2/3	0.6914(169)	12.4(9)	20.3(8)	Fe _{0.51} Ca _{0.35}	20.3
K1	0	0	1/4	2.4(2)	38	K _{2.00}	38
Σ _{EF cations}					108(3)		99
OW7	0.2369(9)	2x	3/4	5.1(2)	40.6(8)		
OW8	0.2553(13)	2x	0.036(15)	10.3(4)	39.8(11)		
OW9	0.490(3)	2x	0.947(2)	10.3(4)	30.0(13)		
OW10	0.4347(8)	2x	0.6733(11)	10.3(4)	61.3(12)	K _{0.40}	7.6
OW11	0.2574(19)	2x	0.588(2)	10.3(4)	37.9(17)		
OW12	0.4299(10)	2x	0.0022(14)	10.3(4)	63.5(15)		
Σ _{water mol.}					273(8)		

Table 5. Relevant bond distances (in Å) and contacts as determined from the Rietveld refinement of the pristine and 500 μM FeCl₂ treated samples. In italic, short contacts.

Site	Bond Distances	Pristine	500 μM FeCl ₂
Ca1	-OW11 ×3	1.75(4)	1.76(4)
	-OW8 ×3	2.42(4)	2.43(4)
	-OW12 ×3	2.53(3)	2.50(3)
	-OW10 ×3	2.76(2)	2.77(2)
	-OW7 ×3	3.43(3)	3.46(3)
	-Ca3	1.70(4)	1.77(4)
	-Ca2	2.45(4)	2.35(4)
Ca2	-OW8 ×3	1.88(3)	1.93(3)
	-OW12 ×3	2.54(3)	2.53(3)
	-OW11 ×3	3.14(4)	3.10(4)
	-O5 ×3	3.38(2)	3.42(3)
Ca3	-OW11 ×3	2.31(4)	2.34(4)
	-OW10 ×3	2.355(19)	2.34(2)
	-OW7 ×3	2.41(2)	2.38(2)
	-OW10 ×3	3.12(2)	3.09(3)
K1	-O2 ×6	2.973(7)	2.952(7)
	-O3 ×6	3.335(7)	3.319(8)

4. Conclusions

The chemical and structural modifications of a sample of fibrous erionite-K were investigated after incubation in a 500 μM FeCl_2 solution. ICP-OES results showed that Fe(II) is fixed by the fibers within the erionite cage (Figure 4) through an ion exchange process mainly involving Ca, among the extra-framework cations. According to the BET specific surface area ($245 \text{ m}^2 \cdot \text{g}^{-1}$) the amount of Fe(II) bound by the fibers was estimated to be of approximately $1.3 \text{ nmol mg}^{-1} \cdot \text{m}^{-2}$, in agreement with that retrieved for the sample from Rome (OR, USA) for which the ion-exchange process mainly affected Na ($1.3 \text{ nmol mg}^{-1} \cdot \text{m}^{-2}$ for the sample incubated in the 500 μM FeCl_2 solution). These data are relevant since the higher selectivity of erionite for Ca with respect to Na provides evidence of the strong tendency of Fe(II) to bind to the erionite structure, owing to its relatively high ionic potential exceeding that of the common extra-framework cations. In addition, considering the marked differences in the extra-framework cation content between woolly erionite-K from Langer County and erionite-Na from Rome (OR, USA) (Figure 3), our results indicate that the efficiency of erionite to bind Fe is not modulated (or weakly modulated) by its chemical composition. As a consequence, considering that the Fe ion-exchanged and/or accumulated on the fiber surface may be responsible for carcinogenic activity promoting the formation of reactive $\text{HO}\bullet$ species via Fenton reaction [75], it is possible that the different erionite species are all potentially carcinogenic. Based on these premises, we are undertaking reactivity and toxicity experiments from the different Fe-loaded erionite species for a dedicated work where we plan to correlate the observed toxicity (and reactivity) with iron topochemistry. Moreover, following the detailed knowledge on the Fe-erionite interaction acquired thus far, further studies are in progress devoted to engineer future roads toward the (at least partial) inactivation of the fibers.

Supplementary Materials: The following are available online at <http://www.mdpi.com/xxx/s1>, Table S1: Experimental details and miscellaneous data of the Rietveld refinements. Statistical parameters as defined in Young [76]. Table S2: Comparison of cell parameters and volume, ϵ_0 microstrain, and principal ellipsoid radii of pristine and Fe(II) loaded samples. For comparison purposes data of woolly erionite-Na from Durkee, Oregon [61] are reported. Table S3: Si, Al partition at T1 and T2 sites and calculation of the R ratio following Jones [72]. List of the uploaded CIF File: CIF file of the pristine sample and of the sample incubated in the 500 μM FeCl_2 solution.

Acknowledgments: The financial support by Sapienza Università di Roma (P.R. Ateneo 2014, Ballirano) is acknowledged. Thanks are due to Andrea Bloise for the TG analysis of the pristine sample.

Author Contributions: Alessandro Pacella conceived the research, performed SEM-EDS, analysed the results, wrote and revised the manuscript; Carlo Cremisini, Elisa Nardi and Maria Rita Montereali engineered and performed binding experiments, carried out ICP-OES measurements, analysed the results, wrote and revised the manuscript; Ida Pettiti performed surface area measurements, analysed the results, wrote and revised the manuscript; Matteo Giordani and Michele Mattioli wrote and revised the manuscript; Paolo Ballirano conceived the research and conducted XRPD experiments, performed structure refinements, analysed the results, wrote and revised the manuscript.

Conflicts of Interest: The authors declare no conflict of interest.

References

1. Sheppard, R.A.; Gude, A.I. Zeolites and associated authigenic silicate minerals in tuffaceous rocks of the Big Sandy Formation, Mohave Country, Arizona. *U.S. Geol. Surv. Prof. Pap.* **1973**, *830*, 36.
2. Tschernich, R.W. *Zeolites of the World*; Geoscience Press: Phoenix, AZ, USA, 1992; p. 563.
3. Bargar, K.E.; Keith, T.E.C. Calcium zeolites in rhyolitic drill cores from Yellowstone National Park. In *Natural Zeolites '93*; Ming, D.W., Mumpton, F.S., Eds.; International Committee on Natural Zeolites, Brockport: New York, NY, USA, 1995; pp. 69–86.
4. Gottardi, G.; Galli, E. *Natural Zeolites*; Springer: Heidelberg, Germany, 1985.
5. Staples, L.W.; Gard, J.A. The fibrous zeolite erionite: Its occurrence, unit cell, and structure. *Mineral. Mag.* **1959**, *32*, 261–281. [[CrossRef](#)]
6. Smith, J.V.; Rinaldi, F.; Dent Glasser, L.S. Crystal structures with a chabazite framework. II. Hydrated Ca-chabazite at room temperature. *Acta Cryst.* **1963**, *16*, 45–53. [[CrossRef](#)]

7. Rüdinger, B.; Tillmanns, E.; Hentschel, G. Bellbergite—A new mineral with the structure type EAB. *Mineral. Petrol.* **1993**, *48*, 147–152. [[CrossRef](#)]
8. Ballirano, P.; Merlino, S.; Bonaccorsi, E.; Maras, A. The crystal structure of liottite, a six-layer member of the cancrinite-group. *Can. Mineral.* **1996**, *34*, 1021–1030.
9. Kawahara, A.; Curien, H. La structure cristalline de l'érionite. *Bull. Soc. Fr. Minéral. Crist.* **1969**, *92*, 250–256.
10. Coombs, D.S.; Alberti, A.; Armbruster, T.; Artioli, G.; Colella, C.; Galli, E.; Grice, J.D.; Liebau, F.; Mandarino, J.A.; Minato, H.; et al. Recommended nomenclature for zeolite minerals; report of the Subcommittee on Zeolites of the International Mineralogical Association, Commission on New Minerals and Mineral Names. *Can. Mineral.* **1997**, *35*, 1571–1606. [[CrossRef](#)]
11. Passaglia, E.; Artioli, G.; Gualtieri, A. Crystal chemistry of the zeolites erionite and offretite. *Am. Mineral.* **1998**, *83*, 577–589. [[CrossRef](#)]
12. Gualtieri, A.; Artioli, G.; Passaglia, E.; Bigi, S.; Viani, A.; Hanson, J.C. Crystal structure-crystal chemistry relationships in the zeolites erionite and offretite. *Am. Mineral.* **1998**, *83*, 590–606. [[CrossRef](#)]
13. Dogan, A.U.; Dogan, M. Re-evaluation and re-classification of erionite series minerals. *Environ. Geochem. Health* **2008**, *30*, 355–366. [[CrossRef](#)] [[PubMed](#)]
14. Crovella, S.; Bianco, A.M.; Vuch, J.; Zupin, L.; Moura, R.R.; Trevisan, E.; Schneider, M.; Brollo, A.; Nicastro, E.M.; Cosenzi, A.; et al. Iron signature in asbestos-induced malignant pleural mesothelioma: A population-based autopsy study. *J. Toxicol. Environ. Health A* **2016**, *79*, 129–141. [[CrossRef](#)] [[PubMed](#)]
15. Lemen, R.A. Mesothelioma from Asbestos Exposures: Epidemiologic Patterns and Impact in the United States. *J. Toxicol. Environ. Health B* **2016**, *19*, 250–265. [[CrossRef](#)] [[PubMed](#)]
16. Barış, Y.I.; Sahin, A.A.; Ozesmi, M.; Kerse, I.; Ozen, E.; Kolacan, B.; Altinörs, M.; Göktepe, A. An outbreak of pleural mesothelioma and chronic fibrosing pleurisy in the village of Karain/Urgüp in Anatolia. *Thorax* **1978**, *33*, 181–192. [[CrossRef](#)] [[PubMed](#)]
17. Dumortier, P.; Coplü, L.; Broucke, I.; Emri, S.; Selcuk, T.; De Maertelaer, V.; De Vuyst, P.; Baris, I. Erionite bodies and fibres in bronchoalveolar lavage fluid (BALF) of residents from Tuzköy, Cappadocia, Turkey. *Occup. Environ. Med.* **2001**, *58*, 261–266. [[CrossRef](#)] [[PubMed](#)]
18. Metintas, M.; Hillerdal, G.; Metintas, S.; Dumortier, P. Endemic malignant mesothelioma: Exposure to erionite is more important than genetic factors. *Arch. Environ. Occup. Health* **2010**, *65*, 86–93. [[CrossRef](#)] [[PubMed](#)]
19. Carbone, M.; Baris, I.; Bertino, P.; Brass, B.; Corertpay, S.; Dogan, A.; Gaudino, G.; Jube, S.; Kanodia, S.; Partridge, C.; et al. Erionite exposure in North Dakota and Turkish villages with mesothelioma. *Proc. Natl. Acad. Sci. USA* **2011**, *108*, 13618–13623. [[CrossRef](#)] [[PubMed](#)]
20. Demirer, E.; Ghattas, C.F.; Radwan, M.O.; Elamin, E.M. Clinical and prognostic features of erionite-induced malignant mesothelioma. *Yonsei Med. J.* **2015**, *56*, 311–323. [[CrossRef](#)] [[PubMed](#)]
21. Coffin, D.L.; Cook, P.M.; Creason, J.P. Relative mesothelioma induction in rats by mineral fibers: Comparison with residual pulmonary mineral fiber number and epidemiology. *Inhal. Toxicol.* **1992**, *4*, 273–300. [[CrossRef](#)]
22. Kokturk, N.; Firat, P.; Akay, H.; Kadilar, C.; Ozturk, C.; Zorlu, F.; Gungen, Y.; Emri, S. Prognostic significance of Bax and Fas ligand in erionite and asbestos induced Turkish malignant pleural mesothelioma. *Lung Cancer* **2005**, *50*, 189–198. [[CrossRef](#)] [[PubMed](#)]
23. Bertino, P.; Yang, H.; Gaudino, G.; Carbone, M. Micro-Raman spectroscopy identifies crocidolite and erionite fibers in tissue section. *J. Raman Spectrosc.* **2013**, *44*, 1440–1445.
24. Zebedeo, C.N.; Davis, C.; Pena, C.; Ng, K.W.; Pfau, J.C. Erionite induces production of autoantibodies and IL-17 in C57BL/6 mice. *Toxicol. Appl. Pharmacol.* **2014**, *275*, 257–264. [[CrossRef](#)] [[PubMed](#)]
25. Baumann, F.; Carbone, M. Environmental risk of mesothelioma in the United States: An emerging concern-epidemiological issues. *J. Toxicol. Environ. Health B* **2016**, *19*, 231–249. [[CrossRef](#)] [[PubMed](#)]
26. Giordani, M.; Mattioli, M.; Dogan, M.; Dogan, A.U. Potential carcinogenic erionite from Lessini Mounts, NE Italy: Morphological, mineralogical and chemical characterization. *J. Toxicol. Environ. Health A* **2016**, *79*, 808–824. [[CrossRef](#)] [[PubMed](#)]
27. International Agency for Research on Cancer (IARC). IARC Monographs on the evaluation of the carcinogenic risk of chemicals to humans. *Silica Some Silic.* **1997**, *42*, 225–239.
28. International Agency for Research on Cancer (IARC). IARC Monographs on the evaluation of the carcinogenic risk to humans. *Arsen. Met. Fibres Dusts* **2011**, *100*, 311–316.

29. Van Gosen, B.S.; Blitz, T.A.; Plumlee, G.S.; Meeker, G.P.; Pierson, M.P. Geologic occurrences of erionite in the United States: An emerging national public health concern for respiratory disease. *Environ. Geochem. Health* **2013**, *35*, 419–430. [[CrossRef](#)] [[PubMed](#)]
30. Ryan, P.H.; Dihle, M.; Griffin, S.; Partridge, C.; Hilbert, T.J.; Taylor, R.; Adjei, S.; Lockey, J.E. Erionite in road gravel associated with interstitial and pleural changes—An occupational hazard in western United States. *J. Occup. Environ. Med.* **2011**, *53*, 892–898. [[CrossRef](#)] [[PubMed](#)]
31. Weissman, D.; Kiefer, M. Erionite—An Emerging North American hazard. NIOSH Science Blog, National Institute for Occupational Safety and Health, 2011. Available online: <http://blogs.cdc.gov/niosh-science-blog/2011/11/erionite/> (accessed on 18 September 2012).
32. Baumann, F.; Buck, B.; Metcalf, R.; McLaurin, B.T.; Merkle, D.; Carbone, M. The presence of asbestos in the natural environment is likely related to mesothelioma in young individuals and women in Southern Nevada. *J. Thorac. Oncol.* **2015**, *10*, 731–737. [[CrossRef](#)] [[PubMed](#)]
33. Kliment, C.R.; Clemens, K.; Oury, T.D. North American erionite-associated mesothelioma with pleural plaques and pulmonary fibrosis: A case report. *Int. J. Clin. Exp. Pathol.* **2009**, *2*, 407–410. [[PubMed](#)]
34. Ilgren, E.B.; Ortega Brena, M.; Castro Larragoitia, J.; Loustaunau Navarrete, G.; Fuentes Breña, A.; Krauss, E.; Fehér, G. A reconnaissance study of a potential emerging Mexican mesothelioma epidemic due to fibrous zeolite exposure. *Indoor Built Environ.* **2008**, *17*, 496–515. [[CrossRef](#)]
35. Ortega-Guerrero, M.A.; Carrasco-Núñez, G. Environmental occurrence, origin, physical and geochemical properties, and carcinogenic potential of erionite near San Miguel de Allende, Mexico. *Environ. Geochem. Health* **2014**, *36*, 517–529. [[CrossRef](#)] [[PubMed](#)]
36. Ilgren, E.B.; Kazemian, H.; Hoskins, J.A. Kandovan the next ‘Capadoccia’? A potential public health issue for erionite related mesothelioma risk. *Epidemiol. Biostat. Public Health* **2015**, *12*, 1–12. [[CrossRef](#)]
37. Passaglia, E.; Galli, E. Levynite and erionite from Sardinia, Italy. *Contrib. Mineral. Petrol.* **1974**, *43*, 253–259. [[CrossRef](#)]
38. Passaglia, E.; Tagliavini, A. Erionite from Faedo, Colli Euganei, Italy. *Neues Jahrb. Geol. Paläontol.* **1995**, *4*, 185–191.
39. Mattioli, M.; Cenni, M.; Passaglia, E. Secondary mineral assemblages as indicators of multistage alteration processes in basaltic lava flows: Evidence from the Lessini Mountains, Veneto Volcanic Province, Northern Italy. *Period. Mineral.* **2016**, *85*, 1–24.
40. Giordani, M.; Mattioli, M.; Ballirano, P.; Pacella, P.; Cenni, M.; Boscardin, M.; Valentini, L. Geological occurrence, mineralogical characterization and risk assessment of potentially carcinogenic erionite in Italy. *J. Toxicol. Environ. Health B* **2017**, *20*, 81–103. [[CrossRef](#)] [[PubMed](#)]
41. Guthrie, G.D. Biological effects of inhaled minerals. *Am. Mineral.* **1992**, *77*, 225–243.
42. Eborn, S.K.; Aust, A.E. Effect of iron acquisition on induction of DNA singlestrand breaks by erionite, a carcinogenic mineral fiber. *Arch. Biochem. Biophys.* **1995**, *316*, 507–514. [[CrossRef](#)] [[PubMed](#)]
43. Carr, A.; Frei, B. Does vitamin C act as a pro-oxidant under physiological conditions? *FASEB J.* **1999**, *13*, 1007–1023. [[PubMed](#)]
44. Fach, E.; Waldman, W.J.; Williams, M.; Long, J.; Meister, R.K.; Dutta, P.K. Analysis of the biological and chemical reactivity of zeolite-based aluminosilicate fibers and particulates. *Environ. Health Perspect.* **2002**, *110*, 1087–1096. [[CrossRef](#)] [[PubMed](#)]
45. Fach, E.; Kristovich, R.; Long, J.; Waldman, W.J.; Dutta, P.K.; Williams, M. The effect of iron on the biological activities of erionite and mordenite. *Environ. Int.* **2003**, *29*, 451–458. [[CrossRef](#)]
46. Matassa, R.; Famigliari, G.; Relucanti, M.; Battaglione, E.; Downing, C.; Pacella, A.; Cametti, G.; Ballirano, P. A Deep Look Into Erionite Fibres: An Electron Microscopy Investigation of their Self-Assembly. *Sci. Rep.* **2015**, *5*, 16757. [[CrossRef](#)] [[PubMed](#)]
47. Gualtieri, A.F.; Bursi Gandolfi, N.; Pollastri, S.; Pollok, K.; Langenhorst, F. Where is iron in erionite? A multidisciplinary study of fibrous erionite-Na from Jersey (Nevada, USA). *Sci. Rep.* **2016**, *6*, 37981. [[CrossRef](#)] [[PubMed](#)]
48. Ballirano, P.; Pacella, A.; Cremisini, C.; Nardi, E.; Fantauzzi, M.; Atzei, D.; Rossi, A.; Cametti, G. Fe(II) segregation at a specific crystallographic site of fibrous erionite: A first step toward the understanding of the mechanisms inducing its carcinogenicity. *Microporous Mesoporous Mater.* **2015**, *211*, 49–63. [[CrossRef](#)]

49. Pacella, A.; Fantauzzi, M.; Atzei, D.; Cremisini, C.; Nardi, E.; Montereali, M.R.; Rossi, A.; Ballirano, P. Iron within the erionite cavity and its potential role in inducing its toxicity: Evidences of Fe (III) segregation as extra-framework cation. *Microporous Mesoporous Mater.* **2017**, *237*, 168–179. [[CrossRef](#)]
50. Pacella, A.; Cremisini, C.; Nardi, E.; Montereali, M.R.; Pettiti, I.; Ballirano, P. The mechanism of iron binding processes in erionite fibres. *Sci. Rep.* **2017**, *7*, 01477. [[CrossRef](#)] [[PubMed](#)]
51. Eberly, P.E. Adsorption properties of naturally occurring erionite and its cationic-exchanged forms. *Am. Mineral.* **1964**, *4*, 30–40.
52. Gude, A.J.; Sheppard, R.A. Woolly erionite from the Reese River zeolite deposit, Lander County, Nevada, and its relationship to other erionites. *Clays Clay Miner.* **1981**, *29*, 378–384. [[CrossRef](#)]
53. Mattioli, M.; Giordani, M.; Dogan, M.; Cangiotti, M.; Avella, G.; Giorgi, R.; Dogan, A.U.; Ottaviani, M.F. Morpho-chemical characterization and surface properties of carcinogenic zeolite fibers. *J. Hazard. Mat.* **2016**, *306*, 140–148. [[CrossRef](#)] [[PubMed](#)]
54. Gutteridge, J.M.C.; Mumby, S.; Quinlan, G.J.; Chung, K.F.; Evans, T.W. Pro-oxidant iron is present in human pulmonary epithelial lining fluid: Implications for oxidative stress in the lung. *Biochem. Biophys. Res. Commun.* **1996**, *220*, 1024–1027. [[CrossRef](#)] [[PubMed](#)]
55. Gregg, S.J.; Sing, K.S.W. *Adsorption, Surface Area and Porosity*, 2nd ed.; Academic Press: New York, NY, USA, 1982.
56. Barrett, E.P.; Joyner, L.G.; Halenda, P.P. The determination of pore volume and area distributions in porous substances. I. Computations from nitrogen isotherms. *J. Am. Ceram. Soc.* **1951**, *73*, 373–380. [[CrossRef](#)]
57. Lippens, B.J.; de Boer, J.H. Studies on pore systems in catalysts: V. The t method. *J. Catal.* **1965**, *4*, 319–323. [[CrossRef](#)]
58. Harkins, W.D.; Jura, G. Surfaces of solids. XII. An absolute method for the determination of the area of a finely divided crystalline solid. *J. Am. Chem. Soc.* **1944**, *66*, 1362–1366. [[CrossRef](#)]
59. Gurvitsch, L. Physicochemical attractive force. *Russ. J. Phys. Chem.* **1915**, *47*, 805–827.
60. Passaglia, E. The crystal chemistry of chabazites. *Am. Mineral.* **1970**, *55*, 1278–1301.
61. Cametti, G.; Pacella, A.; Mura, F.; Rossi, M.; Ballirano, P. New morphological, chemical, and structural data of woolly erionite-Na from Durkee, Oregon, U.S.A. *Am. Mineral.* **2013**, *98*, 2155–2163. [[CrossRef](#)]
62. Bruker AXS. *Topas V4.2: General Profile and Structure Analysis Software for Powder Diffraction Data*; Bruker AXS: Karlsruhe, Germany, 2009.
63. Ballirano, P.; Andreozzi, G.B.; Dogan, M.; Dogan, A.U. Crystal structure and iron topochemistry of erionite-K from Rome, Oregon, U.S.A. *Am. Mineral.* **2009**, *94*, 1262–1270. [[CrossRef](#)]
64. Katerinopoulou, A.; Balic-Zunic, T.; Lundegaard, L.F. Application of the ellipsoid modeling of the average shape of nanosized crystallites in powder diffraction. *J. Appl. Crystallogr.* **2012**, *45*, 22–27. [[CrossRef](#)]
65. Sabine, T.M.; Hunter, B.A.; Sabine, W.R.; Ball, C.J. Analytical expressions for the transmission factor and peak shift in absorbing cylindrical specimens. *J. Appl. Crystallogr.* **1998**, *31*, 47–51. [[CrossRef](#)]
66. Ballirano, P.; Maras, A. In-situ X-ray transmission powder diffraction study of the kinetics of the light induced alteration of realgar (α -As₄S₄). *Eur. J. Mineral.* **2006**, *18*, 589–599. [[CrossRef](#)]
67. Ballirano, P. Effects of the choice of different ionization level for scattering curves and correction for small preferred orientation in Rietveld refinement: The MgAl₂O₄ test case. *J. Appl. Crystallogr.* **2003**, *36*, 1056–1061. [[CrossRef](#)]
68. Chelishchev, N.F.; Volodin, V.F. Ion exchange of alkali metals on natural erionite. *Dokl. Akad. Nauk SSSR* **1977**, *237*, 122–125.
69. Sherry, H.S. Ion-exchange properties of the natural zeolite erionite. *Clays Clay Miner.* **1979**, *27*, 231–237. [[CrossRef](#)]
70. Erdem, E.; Karapinar, N.; Donat, R. The removal of heavy metal cations by natural zeolites. *J. Colloid Interface Sci.* **2004**, *15*, 309–314. [[CrossRef](#)] [[PubMed](#)]
71. Ballirano, P.; Pacella, A.; Bloise, A.; Giordani, M.; Mattioli, M. Thermal stability of woolly erionite-K and considerations about the heat induced behavior of the erionite group. *Minerals* **2018**, *8*, 28. [[CrossRef](#)]
72. Jones, J.B. Al-O and Si-O tetrahedral distances in aluminosilicate framework structures. *Acta Crystallogr.* **1968**, *24*, 355–358. [[CrossRef](#)]
73. Pacella, A.; Ballirano, P.; Cametti, G. Quantitative chemical analysis of erionite fibres using a micro-analytical SEM-EDX method. *Eur. J. Mineral.* **2016**, *28*, 257–264. [[CrossRef](#)]
74. Farrugia, L.J. *ORTEP-3 for Windows*; University of Glasgow: Scotland, UK, 1997.

75. Kamp, D.W.; Weitzman, S.A. The molecular basis of asbestos induced lung injury. *Thorax* **1999**, *54*, 638–652. [[CrossRef](#)] [[PubMed](#)]
76. Young, R.A. Introduction to the Rietveld method. In *The Rietveld Method*; Young, R.A., Ed.; Oxford University Press: Oxford, UK, 1993; pp. 1–38.



© 2018 by the authors. Licensee MDPI, Basel, Switzerland. This article is an open access article distributed under the terms and conditions of the Creative Commons Attribution (CC BY) license (<http://creativecommons.org/licenses/by/4.0/>).